



Cite this: *Phys. Chem. Chem. Phys.*,
2022, 24, 12816

Received 13th April 2022,
Accepted 10th May 2022

DOI: 10.1039/d2cp01712a

rsc.li/pccp

Borophene (B), with remarkably unique chemical binding in its crystallographic structural phases including anisotropic structures, theoretically has high Young's modulus and thermal conductivity. Moreover, it is metallic in nature, and has recently joined the family of two-dimensional (2D) materials and is poised to be employed in flexible hetero-layered devices and sensors in fast electronic gadgets and excitonic devices. Interfacial coupling helps individual atomic sheets synergistically work in tandem, and is very crucial in controllable functionality. Most of the microscopic and spectroscopic scans reveal surface information; however, information regarding interfacial coupling is difficult to obtain. Electronic signatures of dynamic inter-layer coupling in B/boron nitride (BN) and B/molybdenum disulfide (MoS₂) have been detected in the form of distinct peaks in differential current signals obtained from scanning tunneling microscopy (STM) and conducting atomic force microscopy (CAFM). These unique sets of observed peaks represent interfacial coupling quantum states. The peaks in the electronic density of states (DOS) obtained via density functional theory (DFT) band structure calculations matched well with the electronic signatures of coupling quantum states. In our calculations, we found that the DOS peak evolves when the component layers are brought to compromised distances. While B/BN exhibits green sensitivity indicating mid-gap formation, B/MoS₂ bestows red sensitivity indicating band-gap excitation of MoS₂. Molecular detection of methylene blue (MB) based on surface-enhanced Raman spectroscopy (SERS) was carried out with borophene-based hetero-layered stacks as molecular anchoring platforms.

Borophene (B), the lightest elemental Dirac material, has recently become a sensation among the family of two-dimensional (2D) materials.^{1–3} Having the capability of forming

Quantum-coupled borophene-based heterolayers for excitonic and molecular sensing applications†

Kavita Vishwakarma,^{a,b} Shivani Rani,^a Sumit Chahal,^a Chia-Yen Lu,^c Soumya Jyoti Ray,^{ID a} Chan-Shan Yang^{*cd} and Prashant Kumar ^{ID *ae}

three-center-two-electron bonds, boron can form a large number of atomic clusters; as a result, it can have numerous structural phases.⁴ β_{12} and X_3 are two prominent crystallographic phases of borophene, the first one being an anisotropic crystal with atomic ridgelines embedded in it and the second one a flat isotropic hexagonal atomic sheet.⁵ Owing to the anisotropy in its atomic structure, besides being metallic, the β_{12} phase possesses enhanced electronic mobility ($\sim 1.82 \times 10^6 \text{ cm}^2 \text{ V}^{-1} \text{ s}^{-1}$), significantly high Young's modulus ($\sim 398 \text{ N m}^{-1}$) and ferromagnetic properties at room temperature, bolstering its candidature for Flextronics and spintronics.^{5–8} Borophene has been demonstrated to be an excellent material for sensors of gases, light, and tiny molecules and a potential anode material for energy storage devices.^{9,10} Borophene exhibits strong capability as an anodic electrode material that can be used in rechargeable Li-ion batteries (LIBs), Na-ion batteries (SIBs), and Mg-ion batteries (MIBs).^{11,12} Due to the vast range of desired chemical, physical, optical, and electrical properties, borophene is an emergent material for inventing efficient biosensors for diagnostic applications.¹³ Two-dimensional (2D) material-based biosensing, supported by internet-of-medical things (IoMT) and artificial intelligence (AI), has appeared as a new technological platform for intelligent point-of-care (POC) diagnostics. Recently, borophene has emerged as one of such advanced platforms for bioimaging, medical equipment, biosensing applications, cancer treatment along with biocompatibility for future use.^{13–15} A borophene-based wearable sensor can serve as a desired human-to-machine interface for real-time monitoring of electrophysiological parameters (low level $\sim \text{pM}$) in diagnostic applications.¹⁶ Moreover, it has tremendous application potential in plasmonic THz wave guiding as well. Borophene

^a Department of Physics, Indian Institute of Technology Patna, Bihta Campus, Patna-801106, India

^b Department of Electronics and Communication Engineering, Indian Institute of Technology Roorkee, Roorkee-247667, India

^c Institute and Undergraduate Program of Electro-Optical Engineering, National Taiwan Normal University, Taipei 11677, Taiwan. E-mail: csyang@ntnu.edu.tw

^d Micro/Nano Device Inspection and Research Center, National Taiwan Normal University, Taipei 106, Taiwan

^e Global Innovation Centre for Advanced Nanomaterials, The University of Newcastle, University Drive, Newcastle-2308, NSW, Australia.

E-mail: Prashant.Kumar@newcastle.edu.au, magmemory@gmail.com

† Electronic supplementary information (ESI) available. See DOI: <https://doi.org/10.1039/d2cp01712a>

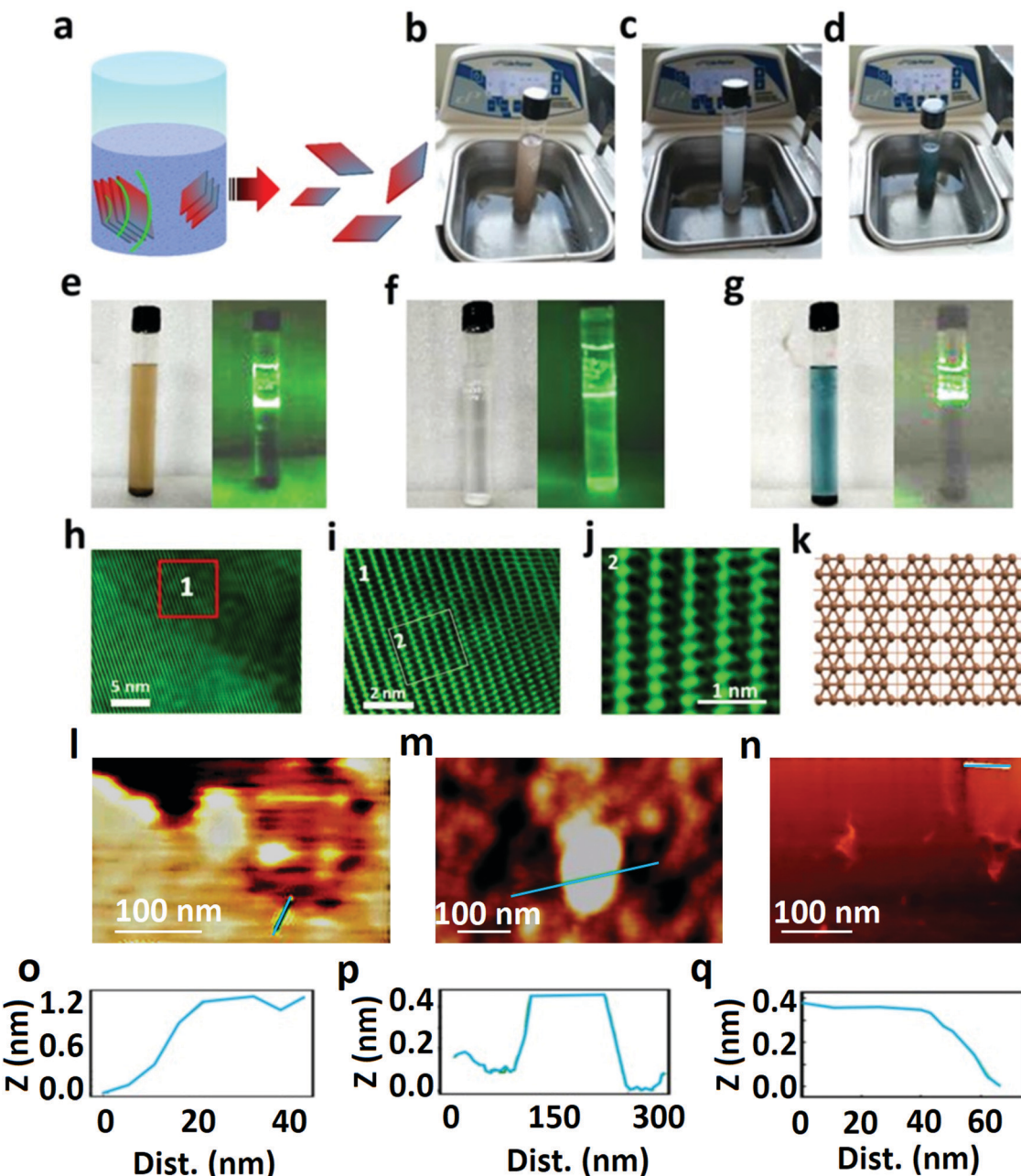


Fig. 1 (a) Schematic diagram of sonochemical exfoliation for the synthesis of 2D materials. Camera photograph of sonochemical synthesis of (b) Borophene, (c) BN and (d) MoS₂. Sonochemically exfoliated samples along with the green light dispersion (Tyndall effect) of (e) borophene, (f) BN and (g) MoS₂. (h) Large-area HRTEM image of synthesized borophene. (i) Zoomed-in HRTEM image of region 1 marked in (h) having ridgelines of atoms and bottom-lying atoms in between two ridgelines correspond to β_{12} of borophene. (j) Zoomed-in HRTEM images of marked region 2 in (i). (k) Schematic atomic diagram of the β_{12} phase. (l and o) AFM image of borophene with a layer height of 1.2 nm. (m and p) AFM image of BN with a layer height of 0.4 nm. (n and q) AFM image of MoS₂ with a layer height of 0.4 nm.

has already been experimentally realized by atomic layer deposition (ALD),¹⁷ molecular beam epitaxy (MBE),¹⁸ chemical vapor deposition (CVD),¹⁹ sonochemical exfoliation (see schematic diagram in Fig. 1(a)),^{9,20} and modified Hummers' method.⁷ Among 2D materials' heterolayers, a G-boron nitride (BN) stack exhibits enhanced electronic mobility due to the atomically smooth and electrostatically clean interface.^{21–27} G-BN stacks have already been applied to electronic tunneling devices and

the manipulation of the photonic emission character of core-shell quantum dots.²⁸ The metallic character of 2D boron makes it complementary to graphene, h-BN, and transition metal dichalcogenides that are bound to serve as ultimate building components in future devices.^{29,30} Inter-layer coupling of heterolayers based on 2D materials, in general, can precisely be tuned with utmost precision, and therefore electronic, photonic, and thermal metamaterials can be fabricated. Inter-layer interactions

between flat atomic sheets give rise to unique quantum states, also termed as electron energy states or pairing states,^{31–34} which assume crucial importance in the research of such novel quantum materials and in the development of emerging applications.

A new member of the family of 2D materials, Borophene has an interface with other 2D materials, the quality of which would be particularly interesting concerning the exploration of future-generation hetero-layered devices and sensors. The enhanced inter-layer coupling between crystalline atomic sheets that constitute heterolayered devices is necessary for out-of-plane information processing. Clean material interfaces are mandatory for efficient data transfer. Defects, vacancies, and oxygen functionalities at the interfaces are undesirable; therefore we opted for the sonochemical approach of synthesis for 2D sheets. We have strived to develop a better understanding of the resulting quantum states and excitonics occurring at the B/BN and B/MoS₂ interfaces and to further exploit this for practical applications. The resulting surfaces and interfaces were characterized by employing field-emission scanning electron microscopy (FESEM), transmission electron microscopy (TEM), and atomic force microscopy (AFM), and spectroscopic (UV-Vis and Raman) tools. The electronic characters of hetero-layered interfaces were investigated by conductive atomic force microscopy (CAFM) and scanning tunneling microscopy (STM). To explore the presence of quantum states, the differential current *vs.* voltage curve was analyzed. To validate the origin of such quantum states in differential spectra, DFT band structure calculations were performed for heterolayers at different distances (*viz.* 2 Å and 2.5 Å) and equilibrium distances (3.77 Å for B/BN and 3.28 Å for B/MoS₂, respectively). Electronic band structures, the density of states, LUMO–HOMO (lowest unoccupied molecular orbital–highest occupied molecular orbital), and charge density difference profiles were attained. To explore the excitonic behaviour of heterolayers, photoconductivity measurements were carried out. Molecular detection based on surface-enhanced Raman spectroscopy (SERS) was conducted for methylene blue (MB) with various heterolayers including MB/B/BSG (Borosilicate glass), MB/B/BN/BSG, and MB/B/MoS₂/BSG.

Methods

Synthesis of borophene and other 2D materials

Sonochemical synthesis of 2D materials was carried out using an ultra-sonicator (Cole Parmer) working at a frequency of 40 kHz under the processing condition at room temperature for 12–20 hours with IPA (isopropyl alcohol) as a solvent. The solution obtained after prolonged sonication was left to stand for four hours and was then centrifuged at 10 krpm for six minutes (camera images in Fig. S1, ESI†). Washing steps involved centrifugation in DI (deionized water) water (two times), ethanol, and 17% HCl, again with DI water and finally with ethanol each at 10 krpm and for six minutes. Upon centrifugation, the solution in the centrifugation tube was transferred to another container, and the supernatant (*i.e.* top 1/3 of the solution) was removed to another vial that was used for further characterization.

Characterization of synthesized 2D materials

A Raman spectrometer equipped with an integrated microscope from Olympus (Seki Techno Tron Corporation, Japan) was used for optical microscopy, and a He–Ne laser with a wavelength of 633 nm was used to record Raman spectrographs of the spin-coated film on silicon substrates at room temperature. An atomic force microscope (Agilent Model No. 5500) was used to capture topography in the non-contact dynamic force mode. UV-Vis spectroscopy (SHIMADZU UV-2600) of 2D materials dispersed in IPA was carried out under ambient conditions in a quartz cuvette. A Tauc plot was used to obtain bandgaps of 2D materials. Transmission electron microscopy was carried out using a JEOL JEM 2100 to acquire high-resolution images and selected area electron diffraction (SEAD) patterns of the synthesized 2D sheets.

CAFM and STM measurements

Scanning tunneling microscopy, which is capable of real-time tunneling current measurement, was carried out with an STM tip at a distance of ~5 Å from the surface of the sample (this distance is in the range of equilibrium distance). Mild bias up to 1 V was applied, and it yielded the tunneling current. The tunneling current is primarily determined by the density of states (DOS) of a material's surface, the material of the tip and geometric and thermal conditions. We conducted all measurements with the same tip and at the same room temperature, and therefore, any difference in the tunneling current was inferred to occur due to the sample's local electronic behaviour (local density of states). CAFM, in contrast, had a different tip, and the measurement was done in the contact mode. To acquire information on the local electronic behaviour in an indisputable manner, both STM and CAFM were carried out on all heterolayers. Gold-coated (DC sputtered) silicon substrates were used for the subsequent transfer (by spin-coating) of a heterolayer, which was eventually used for STM/CAFM measurements. An adequate drying protocol (100 °C for 20 min.) was followed. Current *vs.* voltage *via* CAFM and STM of borophene, B/BN heterolayers, and B/MoS₂ heterolayers is shown in Fig. S7, ESI.†

Photoconductivity measurements

Photoconductivity measurements were carried out under ambient conditions with two-probe measurements. Wet chemical lithography was employed to obtain electrode pads with a distance of ~10 μm. While cleaning the device, 2D materials were coated in the gap *via* spin-coating and then adequately dried on a hot plate at 120 °C for half an hour. Molybdenum electrode pins were used for *I*–*V* measurements in a Keithley source meter (model no. 2634 B). Blue, green, and red lasers at wavelengths of 405 nm, 532 nm, and 650 nm, respectively, were used to optically excite the material for photoconductivity measurements.

SERS measurements

Two-dimensional sheets of borophene and borophene-based heterolayers were coated onto gold-sputtered borosilicate glass (BSG) substrates (see the schematic diagram in Fig. 5(d)). Methylene blue

molecules (100 ppm solution) were then transferred by drop-casting over it, and then an adequate drying protocol was followed. A He-Ne red laser with a wavelength of ~ 633 nm with a moderate power level (~ 5 mW) was employed in a Raman instrument. The results obtained considering heterolayers as substrates were compared with those considering borophene as the substrate.

Computational details

First-principles-based density functional theory (DFT) calculations were used to determine the electronic structure of borophene and its van der Waals (vdw) heterostructure with MoS₂ and BN. Self-consistent calculations (SCC) were obtained using the Perdew–Burke–Ernzerhof (PBE) exchange-correlation functional employing the generalized gradient approximation (GGA).³⁵ Semi-empirical corrections by Grimme D2 and D3 were included within the GGA in order to account for van der Waals interactions. A Monkhorst-pack *k*-grid of $3 \times 4 \times 1$ was employed for sampling the Brillouin zone. The wave functions were expanded into a double- ζ polarized (DZP) basis set and 500 eV was set as the cutoff energy limit. The structural optimization was duly performed until the force on each atom was less than 10^{-6} eV Å⁻¹ under various conditions.

Results and discussions

Microscopy and spectroscopy of individual layers

Even though bulk boron is black and its monolayer is optically transparent, moderate concentration in the supernatant obtained after sonochemical exfoliation in isopropyl alcohol (IPA) followed by centrifugation showed brownish shade (see Fig. 1(b and e)). Similarly, monolayers of BN and MoS₂ are optically transparent. However, the supernatant obtained with a few layers of BN and MoS₂ exhibited whitish and bluish shades, respectively (see Fig. 1(c, d) and (f, g)). AFM imaging revealed sheet-like features in borophene, BN and MoS₂ (see Fig. 1(l-n) respectively). Line profiles obtained further revealed a typical lateral dimension in a 40–300 nm range and a typical height of 0.4–1.2 nm, which confirms the presence of 1–3 monolayers of 2D sheets (see Fig. 1(o-q); lateral dimension and thickness distribution (see ESI† Fig. S3(a, b) borophene (c, d) B/BN, and (e, f) B/MoS₂)). Raman fingerprints of borophene (~ 716 cm⁻¹), BN (~ 1367 cm⁻¹), and MoS₂ (~ 382 and ~ 406 cm⁻¹) proved their chemical phase purity (see Fig. 2(d, h and l)). UV-Vis spectroscopy of the borophene supernatant exhibited no absorption peak in the visible range, indicating its optically transparent nature (see Fig. S2(a), ESI†). In contrast, BN and MoS₂ exhibited absorption peaks in the UV region and the visible range, respectively (see Fig. S2(b and c), ESI†). A Tauc plot revealed the band gaps of 4.5 eV and 1.67 eV for BN and MoS₂, respectively, which confirmed the presence of monolayers and few layers of these 2D materials, thus validating that exfoliation has occurred. Inter-layer interactions between borophene and boron nitride can easily be captured by Raman spectroscopy in the form of peak shifts (see Fig. S4, ESI†). Sonochemically exfoliated borophene in an IPA solvent is

highly crystalline. Large-area HRTEM image (see Fig. 1(h)) of synthesized borophene along with the zoomed-in images of marked regions 1 and 2 is shown in Fig. 1(i and j) respectively, showing top-lying ridgelines of atoms and bottom-lying atoms in between two ridgelines corresponding to β_{12} of borophene (schematic atomic diagram of the β_{12} phase is shown in Fig. 1(k)). Moreover, resolved TEM images in Fig. 2(b) from Fig. 2(a) appear to be Moiré's pattern. Moreover, a four-fold symmetry is evidenced from selected area fast Fourier transform (FFT) (see the inset in Fig. 2(b)). We can summarize that due to multilayer stacking, Moiré's pattern develops. In fact, borophene has two predominant crystallographic phases— β_{12} (atomic ridge lines separated by low-lying atoms) and X_3 (the planar phase). Similar to borophene, BN and MoS₂ were synthesized via sonochemical synthesis in an IPA solvent. Interestingly, BN exhibited a hexagonal phase as apparent as it is in high-resolution transmission electron microscopy (HRTEM) imaging (see Fig. 2(f) resolved from Fig. 2(e)). FFT (see the inset in Fig. 2(f)) demonstrates a six-fold symmetry. The average inter-atomic distance is 3 Å along the linear chain and 2.7 Å normal to it (shown in Fig. 2(g)). HRTEM imaging for synthesized MoS₂ sheets shows arrays of atoms, and the local FFT exhibits a two-fold symmetry (see Fig. 2(j) a section of Fig. 2(i)). Average inter-atomic distances along the chain and normal to it were 2.9 Å and 2.6 Å respectively (see Fig. 2(k)). Inter-atomic distances indicate that the atomic structures in the HRTEM image do not represent the nearest neighbors (atoms) due to poor resolution. Thus, crystalline phases of synthesized 2D materials and the nature of symmetry and symmetry directions have been recognized. The presence of strain and defects in synthesized sheets is minimal; however, it cannot be ruled out. The 3D atomic views of B, BN, and MoS₂ obtained through HRTEM are shown in Fig. 2(b, f and j), respectively.

STM and CAFM measurements

Inter-layer coupling is crucial in determining in-plane inter-atomic distances and the underlying crystallographic symmetry in 2D materials, determining the overall quantum mechanical behaviour of the system. In hetero-layered devices composed of borophene over another 2D material, *e.g.*, BN or MoS₂, inter-layer coupling and its interplay in determining quantum states would be worth observing, especially its impact on electronic and excitonic behaviour. Further details of how electronically the hetero-layered materials behave were captured by conducting atomic force microscopy and scanning tunneling microscopy. While borophene on the Au substrate exhibits an appreciable current of ~ 1.5 nA (see Fig. 3(a) and line profile in Fig. 3(b)) with almost uniform current profile (see 3D view in Fig. 3(c)), borophene on MoS₂ exhibits a comparatively reduced current of ~ 0.8 nA (see Fig. 3(d) and line profile in Fig. 3(e)) with a non-uniform profile as apparent from spikes in current (see 3D view in Fig. 3(f)). Borophene on BN, in contrast, exhibits the lowest current of ~ 0.7 nA (see Fig. 3(g) and line profile in Fig. 3(h)) with a completely non-uniform current profile and current being observed at rare locations (see 3D view in Fig. 3(i)).

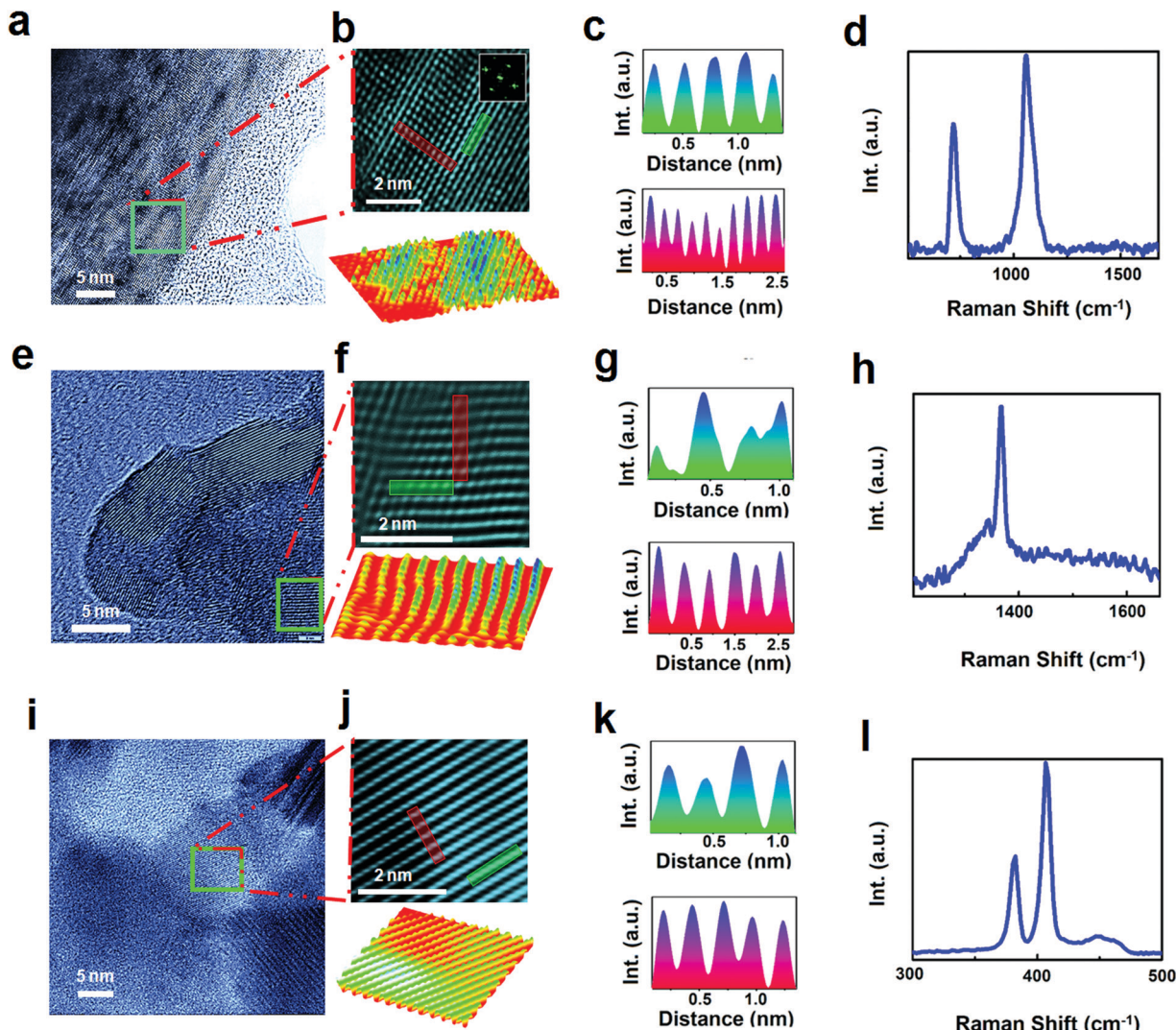


Fig. 2 HRETM and Raman characterization. (a) TEM image of borophene. (b) HRTEM image along with a corresponding 3D view of borophene (with inset FFT). (c) Atomic line profiles along the ridgeline (green) and normal to it (red) shown in (b). (d) Raman identification of borophene. (e) TEM image of BN. (f) HRTEM image of BN along with 3D atomic view. (g) Atomic line profiles along the array of an atom (green) and normal to it (red) shown in (f). (h) Raman characterization of BN. (i) TEM image of MoS₂. (j) HRTEM image of MoS₂ and its 3D view. (k) Line profile along with the array of atoms (green) and normal to it (red) shown in (j). (l) Raman fingerprint of MoS₂.

Observed current values exclusively depend on the electronic character of top and bottom layers, their band alignment, stacking sequence, defects and strain in the systems. Observed current profiles on the borophene-based heterolayers speak about the uniformity or non-uniformity of current over a selected area, which depends on several factors, primarily on how the top layer was integrated into the underlying bottom layer or substrate and also on stray charges developed at the surface and interfaces.

It should be noted that the STM tunneling signal follows the Fowler–Nordheim behaviour (see Fig. S5, ESI†). We obtained distinct CAFM and STM peaks representing quantum mechanical electronic signatures. While borophene exhibited CAFM peaks at -0.456 V, -0.535 V, and -0.717 V (see Fig. 4(b) blue plot), STM measurements on the same sample reveal peaks at -0.399 V, -0.49 V, and -0.688 V (see Fig. 4(b) red plot, and

schematic diagram of measurements is shown in Fig. 4(a)). However, B/BN heterolayer (see schematic diagram in Fig. 4(e)) stacks exhibited CAFM peaks at -0.181 V, -0.304 V, and -0.430 V (see Fig. 4(f) blue plot). In contrast, the same B/BN heterolayer exhibited STM peaks at -0.0229 V and -0.156 V (inset in Fig. 4(f) red plot). In order to investigate how CAFM/STM peaks are altered when BN is replaced by MoS₂, a B/MoS₂ heterolayer was fabricated (see the schematic diagram in Fig. 4(j)). B/MoS₂ exhibited CAFM peaks at -0.595 V, -0.3927 V, -0.409 V, 0.584 V, and 0.788 V (inset in Fig. 4(j) blue plot). Similarly, while B/MoS₂ exhibited STM peaks at -1.109 V, -0.856 V, -0.647 V, -0.421 V, 0.018 V, 0.18 V, and 0.219 V (inset in Fig. 4(j) red plot). Surprisingly, some of the STM and CAFM peaks were common. It was surprising to observe sharp peaks in current signals using both STM and CAFM in hetero-layered systems, which we attribute to enhanced interactions between the 2D materials.

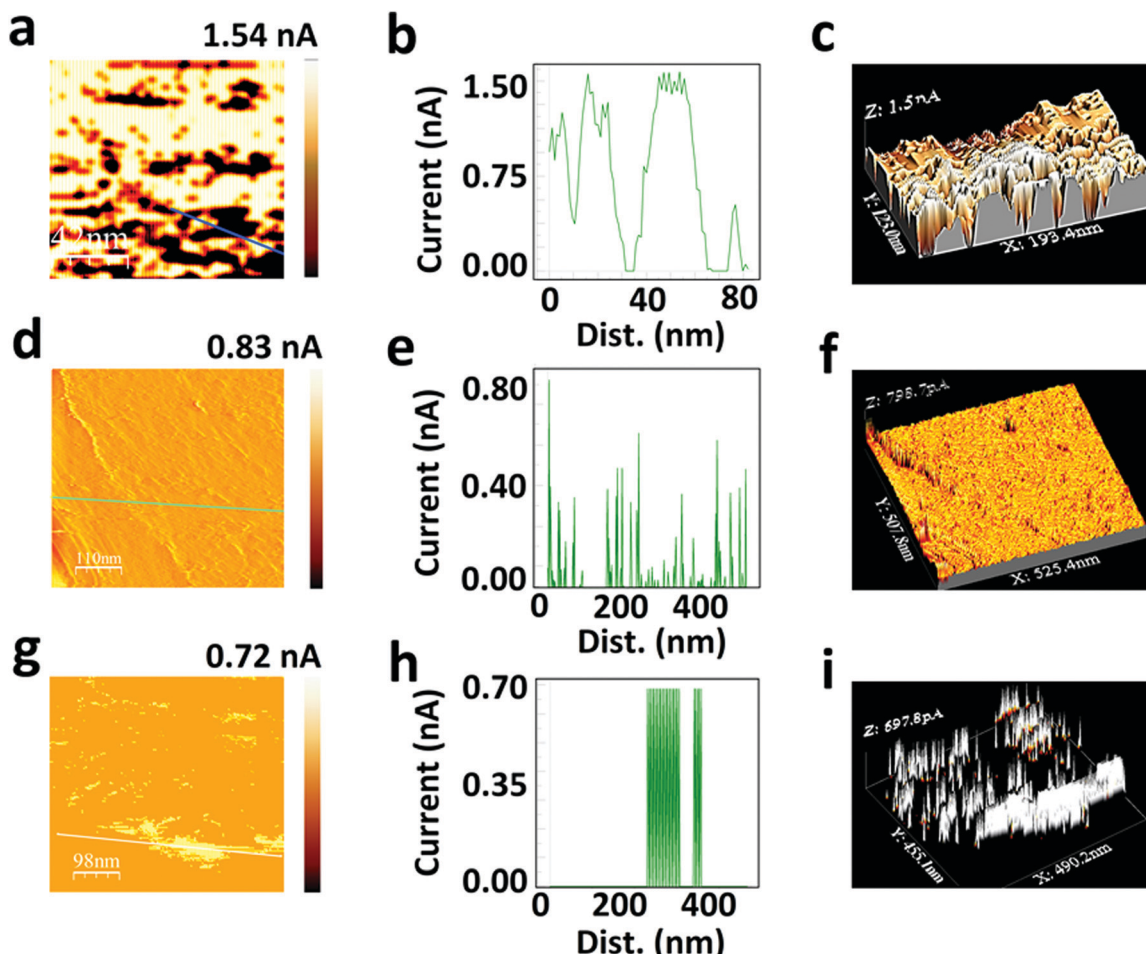


Fig. 3 CAFM image for (a) B/Au, (d) B/MoS₂, and (g) B/BN. Corresponding line profiles for marked lines for (b) B/Au, (e) B/MoS₂, and (h) B/BN. Corresponding 3D view of images for (c) B/Au, (f) B/MoS₂, and (i) B/BN.

DFT calculation of coupling states

In order to have a better understanding of the origin of CAFM/STM electronic signatures, it was imminent to carry out electronic band structure calculations for 2D-material hetero-layered stacks including B/BN and B/MoS₂. Borophene is metallic in nature (the band structure and DOS shown in Fig. 4(c and d); see details in Fig. S6 and S7, ESI†). When B and BN atomic sheets were brought closer, inter-layer coupling enhances, which results in peaks in electronic density of states (DOS). In practicality, 2D materials placed over each other will not statistically maintain the same distance and, therefore, we calculated DFT band structures for different inter-layer distances, namely, 2, 2.5 and 3.77 Å in the case of B/BN and 2, 2.5 and 3.28 Å in the case of B/MoS₂ (see details in Fig. S8–S15, ESI†). Band structures of hetero-layered stacks demonstrate distinct electronic states (peaks in DOS) at a particular inter-layer distance (see Fig. 4(g, k) and (h, l)). Side view of HOMO and LUMO orbital profile of borophene, B/BN and B/MoS₂ are shown in Fig. 5(a, b), (e, f) and (i, j) and the corresponding energy diagram in Fig. 5(c, g and k) respectively. Inter-layer coupling can be seen from the profile of charge density difference and at a distance of 2 Å, and we could see the

overlap of orbitals (see Fig. 5(d, h and l)). Such integral coupling will homogenize electrostatic surface charge,¹⁸ moreover, enhanced optical transparency is expected.²⁴ This result further vindicates our findings of Raman peak shifts for B and BN in hetero-layered stacks as compared to those for individual layers. Band structures, DOS, and charge density difference profiles for the inter-layer distances of 2.5 Å and other distances are shown in Fig. S9–S14 (ESI†). When theoretical peak positions in the DOS were indexed on experimental CAFM and STM plots for B/BN and B/MoS₂, observed electrical signals matched theoretical positions for different inter-layer distances. Such observations point to the dynamic nature of hybridization between PZ orbitals of B and those of BN and MoS₂. Thus, while 2D materials tend to be at equilibrium distances (3.77 and 3.28 Å for B/BN and B/MoS₂, respectively) if no external force is applied, fabrication processing (e.g. heating) would bring the individual 2D materials even at compromised (less than the equilibrium) distances.

Perspective on evolution of coupled 2D material systems

G/BN heterolayers have already been demonstrated to exhibit excellent device functionality in contrast to G/SiO₂.³⁶ Lattice

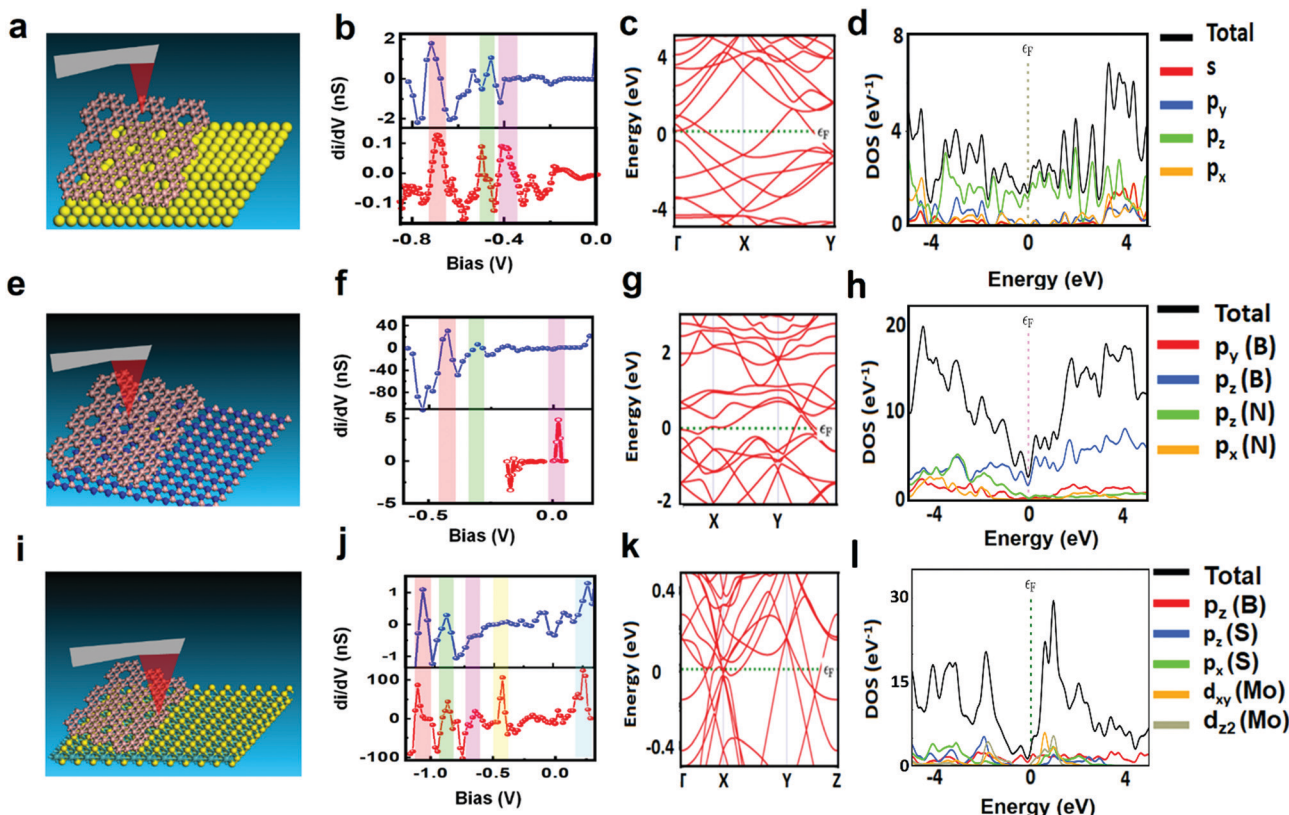


Fig. 4 CAFM and STM measurements along with DFT calculations. (a) Schematic diagram of borophene over a gold-sputtered silicon substrate. (b) Obtained plots of dI/dV vs. voltage of CAFM (blue) and STM (red), both plots showing matches of almost all peaks. (c) DFT band structure (dotted green line corresponds to the Fermi-level) and (d) DOS calculations for borophene. (e) Schematic diagram of B/BN heterolayers over a gold-sputtered silicon substrate. (f) Obtained plots of dI/dV vs. voltage of CAFM (blue) and STM (red). (g) DFT band structure and (h) DOS calculated for B/BN heterolayers. (i) Schematic diagram of B/MoS₂ heterolayers over a gold-sputtered silicon substrate. (j) Obtained plots of dI/dV vs. voltage of CAFM (blue) and STM (red). (k) DFT band structure and (l) DOS calculations for B/MoS₂ heterolayers.

mismatch of graphene with BN is $\sim 1.7\%$, which reduces charge fluctuation from 10^{12} to 10^9 cm^{-2} .³⁷ It should be noted that BN is an excellent electronic tunneling barrier. It supports carrier injection up to 6 monolayers.^{28,32} Multilayer BN ($\varepsilon \sim 3\text{--}4$) has been used in FET, memristors, etc. The breakdown field for the BN barrier in G/BN hetero-layered electrical devices is $\sim 0.8 \text{ V nm}^{-1}$. The integral and fractional quantum Hall effects and the spin quantum Hall effect have been demonstrated in G/BN heterolayers.³⁸ G/BN heterolayers form Moiré patterns where orbital hybridization is prominent and due to sub-lattice symmetry breaking, the bandgap opens (tunable with twist angle) at the Dirac point.³⁸ The evolution of the bandgap occurs in order to structurally relax for overcoming the stacking potential.³² Interestingly, twisted commensurate flat atomic sheets G/G, G/BN, etc., have recently been discovered to be superconducting.^{39,40} Moreover, when BN interfaces with MoS₂, it will modulate its band structure and, hence, can alter its optical behaviour. Orbital hybridization of BN-MoS₂ leads to the up-shift of the valence band.⁴¹ Exploring Moiré heterolayers has become a treasure hunt off late.⁴² With all these recent developments in hetero-epitaxial and twistrionic devices composed of Xenes, metal dichalcogenides, insulating BN and other emerging atomic sheets, recently discovered borophene is poised to catch up its momentum and

exhibit its flavors, which are expected due to its unique binding capabilities and metallic nature. BN in proximity to borophene will block extrinsic disorders (passivate scattering centers), and hence, it would enhance electronic mobility. Low-power electronic and optoelectronic devices working at THz frequencies, light-emitting diodes, and thermal detectors can be fabricated using B/BN and B/MoS₂-based heterolayers. Enormous opportunities can be found in these new-age devices and sensors, and it is the right timing for borophene as concerned device physics has already been developed. It should be noted that borophene-based Moiré structures have never been explored to date, but they have tremendous possibilities. In borophene-based heterolayers, inter-layer coupling as revealed by quantum mechanical signatures will be determined by the inter-layer distance as well as twist angles.

Hamiltonian for inter-layer coupling⁴³

$$U(\tilde{k}, k) = \frac{1}{N} \sum_{\tilde{G}} t_{\tilde{X}X}(\tilde{k} + \tilde{G}) e^{i\tilde{G} \cdot \tau_{\tilde{X}}} \sum_{R_X} e^{i(k - \tilde{k} - \tilde{G}) \cdot R_X}$$

where k and \tilde{k} are the Bloch wave vector of two layers of the heterostructure. G and \tilde{G} are the reciprocal lattice vector, R_X is

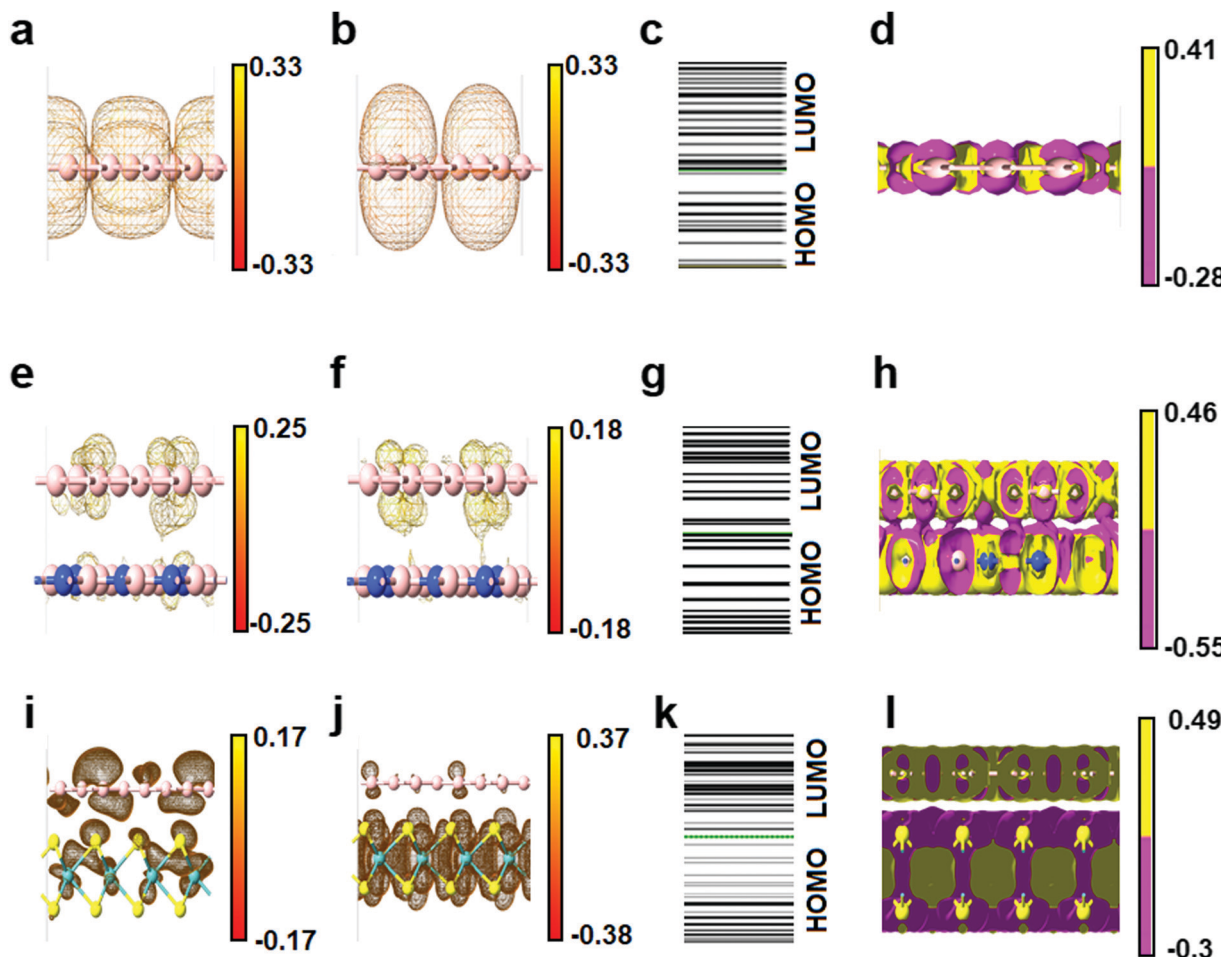


Fig. 5 HOMO/LUMO and charge density profiles. Schematic diagram of the side view of (a) HOMO and (b) LUMO orbital profiles of borophene. (c) LUMO/HOMO energy diagram (dotted green lines correspond to the Fermi level) and (d) charge density difference profile of borophene. Schematic diagram of the side view of (e) HOMO and (f) LUMO orbital profile of the B/BN heterolayer. (g) LUMO/HOMO energy diagram and (h) charge density difference profile of the B/BN heterolayer. Schematic diagram of the side view of (i) HOMO and (j) LUMO orbital profiles of the B/MoS₂ heterolayer. (k) LUMO/HOMO energy diagram and (l) charge density difference profile of the B/MoS₂ heterolayer.

the lattice position vector, τ_x and $\tau_{\bar{x}}$ are the sub-lattice position vector of two layers and t_{xx} is the Fourier transform integral.

With local 3D straining and shearing, graphene assumes novel quantum electronic states.^{31,44,45} Stacking heterolayers of 2D materials create opportunities for accessing novel electronic and excitonic behaviours in a tunable manner, and hence, electronic metamaterials can be realized.^{31,32,45,46} The mobility of graphenes has been reported to be significantly enhanced when integrated with BN substrates.⁴¹ The local electronic response of the graphene/BN heterolayer has been investigated by STM.^{22,36,37} Our STM and CAFM-based research findings on the manipulation of local electronic behaviour in B/BN and B/MoS₂ hetero-layered stacks prove inter-layer coupling and, hence, significant charge transfer. DFT band structure calculations enormously enhanced peaks in DOS and orbital hybridization; evidence from the charge density difference profiles supports our experimental findings.

Photoconductivity measurements

Having proven electronically excited states in B/BN and B/MoS₂ hetero-layered stacks, we conducted photoconductivity

measurements to access photo-excited states of these heterolayers (see Fig. 6(a–c)). The negative photoconductivity effect is connected to trap centers, surface gas molecules and surface plasmons, photo thermal effects, photovoltaic effects, etc., in low-dimensional materials. Two-dimensional materials have exceptional chemical and physical properties, a large specific surface area, a high surface electron concentration, and abundant surface states. Therefore, the low-dimensional materials are more conducive to the generation of traps, the adsorption, as well as the excitation of the surface plasmons. The formation process of the negative photoconductivity effect caused by the trapping effect can be simply understood as the trap centers capturing photo-induced carriers, causing the conductivity to decrease.⁴⁷ We observed negative photoconductivity that was attributed to the photo-thermal effect at the interfaces of the 2D materials when an incident ray of light hit the interfaces. The heat generated at the interface enhanced electronic scattering, and hence, electrical signals were reduced. Negative photoconductivity has been reported in van der Waals hetero-layered stacks.⁴⁸ An individual borophene layer responded to light

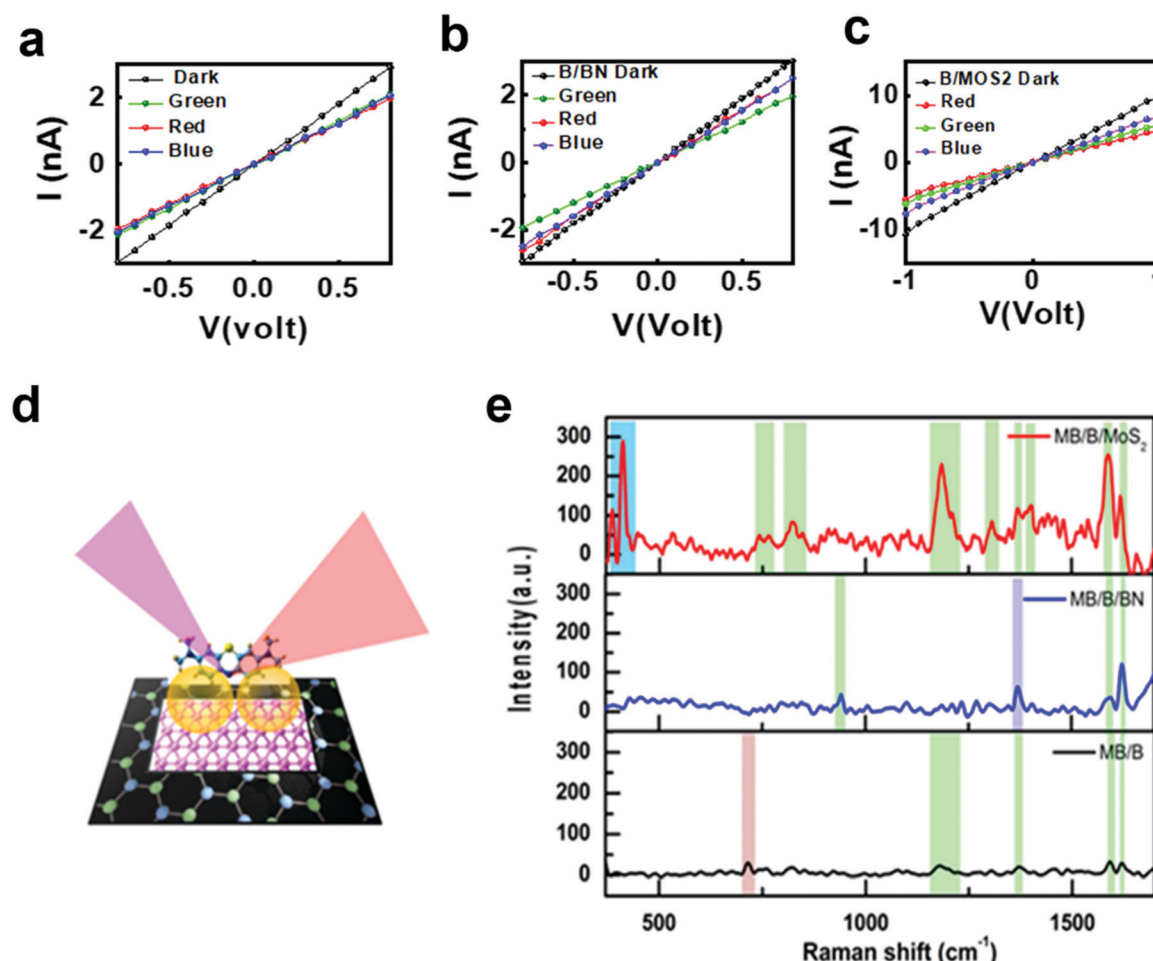


Fig. 6 Current vs. Voltage (I - V) and photoconductivity (PC) measurements for (a) borophene, (b) B/BN heterolayer and (c) B/MoS₂ heterolayer. (d) Schematic diagram of SERS for molecular sensing on Gold sputtered BSG. (e) Experimentally obtained surface-enhanced Raman peaks of methylene blue drop-casted over for B, B/BN, and B/MoS₂ heterolayers.

intensity and resulted in negative photoconductivity. However, it was wavelength insensitive. For B/BN heterolayers, green laser excitation resulted in maximal effects (implicating at mid-gap formation); for B/MoS₂, red laser exhibited significantly more impact (as MoS₂ is red-sensitive). Thus, we could access electronically as well as optically excited states in borophene-based heterolayered stacks. The negative photoconductivity has potential applications in optoelectronic detection, optoelectronic switching, optoelectronic memory, gas detection, and so on. For example, the negative photoconductivity effect is beneficial to expand the functions of traditional photoelectric detection and is anticipated to be applied to low-power, high-speed frequency response photodetectors.^{49,50}

Heterolayers as anchors for SERS-based molecular sensing

Molecular sensing through surface-enhanced Raman scattering (SERS) has a real-life application that has never been realized yet for borophene-based heterolayers. Besides the molecular anchoring capability of borophene due to the presence of atomic ridgelines, borophene sheets are electronically metallic as well as thermally conductive, which will help promptly

remove heat generated at the interfaces. As SERS involves the light-matter interaction, our natural curiosity lies in whether such heterolayers can creatively be used for molecular sensing *via* SERS. To our surprise, hetero-layered stacks show superior Raman signals for methylene blue (MB) molecules anchored on it. Raman peaks corresponding to the substrates used in SERS experiments have all been shaded viz. Raman peak for Borophene \sim 716 cm⁻¹; peak for BN \sim 1367 cm⁻¹; peak for MoS₂ \sim 384, 412 cm⁻¹. SERS signals from MB were observed at 1178, 1367, 1587, and 1623; for B, at 942, 1594, and 1622 cm⁻¹; for B/BN at 756, 824, 1184, 1305, 1369, 1404, 1589, and 1619 cm⁻¹ for B/MoS₂ (see Fig. 6(d and e)). It was interesting to note that B/MoS₂ as the interface resulted in superior Raman enhancement to that of the B/BN heterolayer. However, with BN and MoS₂ as substrates, there are preferential enhancements for particular peaks of MB.

Conclusions

Borophene-based hetero-layered stacks have been fabricated with 2D materials, BN and MoS₂. Electronic signatures of

quantum states in B/BN and B/MoS₂ hetero-layered systems were captured *via* CAFM/STM and we could find peaks in differential current signals. Strong interlayer coupling is responsible for sharp peaks. Noises were almost absent in most of the measurements, but if there are any noises, they are negligible. Peaks in DOS obtained from our DFT band structure calculations closely matched with the experimental peaks in differential electronic signatures of inter-layer coupling quantum states. It turned out that the hetero-layered systems exhibited dynamic inter-layer coupling. At the moment when quantum states are captured through their electronic signatures, atomic configurations in two atomic crystals facing each other would be very unique. However, distances between atoms speak of orbital-overlaps and hence the strength of out-of-plane binding. Ground states and excited states (electric/optical) in the energy landscape for the Moiré heterolayers will be quantum mechanically defined and the system can assume of such discrete states, depending on the external source of excitation. Optically excited states were also experimentally explored employing photoconductivity measurements. Interestingly, while B/BN exhibits green sensitivity (implying at mid-gap formation), B/MoS₂ exhibits red sensitivity (as MoS₂ becomes photoactive when excited at its band-gap energy). Light-matter interactions at the B/BN and B/MoS₂ interfaces have been exploited for the molecular detection of methylene blue *via* SERS. We believe that the research findings in this article will lead to future generations of borophene-based hetero-layered electronic and excitonic devices and sensors.

Author contributions

P. K. conceived the idea; K. V. carried out synthesist of borophene, B. N. and MoS₂ and fabricated heterolayers and employed STM and CAFM measurements; S. C. helped with characterization of individual 2D materials; S. R. completed DFT band structure calculations under the supervision of S. J. R. S. C., C. S. Y., and P. K. wrote the manuscript together. We discussed the manuscript and experimental results with C. Y. L. and C. S. Y. The project was overall supervised by P. K.

Conflicts of interest

There is no conflict of interests.

Acknowledgements

The authors acknowledge the financial support from the Department of Science and Technology (DST), Govt. of India and The University of Newcastle, Australia. Authors acknowledge financial support from SERB, Govt of India (SB/S2/RJN-205/2014) and Ministry of Science and Technology Taiwan (110-2112-M-003-012-MY3).

References

- A. J. Mannix, Z. Zhang, N. P. Guisinger, B. I. Yakobson and M. C. Hersam, *Nat. Nanotechnol.*, 2018, **13**, 444–450.
- P. Ranjan, J. M. Lee, P. Kumar and A. Vinu, *Adv. Mater.*, 2020, **32**, 2000531.
- Z. Lin, A. McCreary, N. Briggs, S. Subramanian, K. Zhang, Y. Sun, X. Li, N. J. Borys, H. Yuan and S. K. Fullerton-Shirey, *2D Mater.*, 2016, **3**, 042001.
- L. Burnelle and J. J. Kaufman, *J. Chem. Phys.*, 1965, **43**, 3540–3545.
- Z. Q. Wang, T. Y. Lü, H. Q. Wang, Y. P. Feng and J. C. Zheng, *Front. Phys.*, 2019, **14**, 1–20.
- S. Tomar, P. Rastogi, B. S. Bhadaria, S. Bhowmick, A. Agarwal and S. Y. Chauhan, IEEE International Conference on Electronics, Computing and Communication Technologies (CONECCT), IEEE: 2018, 1–4.
- C. L. Zou, D. Q. Guo, F. Zhang, J. Meng, H. L. Miao and W. Jiang, *Syst. Nanostruct.*, 2018, **104**, 138–145.
- Z. Zhang, Y. Yang, E. S. Penev and B. I. Yakobson, *Adv. Funct. Mater.*, 2017, **27**, 1605059.
- P. Ranjan, T. K. Sahu, R. Bhushan, S. S. Yamijala, D. J. Late, P. Kumar and A. Vinu, *Adv. Mater.*, 2019, **31**, 1900353.
- S. Chahal, P. Ranjan, M. Motlag, S. S.-R. K.-C. Yamijala, D. J. Late, E. H.-S. Sadki, G. J. Cheng and P. Kumar, *Adv. Mater.*, 2021, **33**, 2102039.
- Y. Zhang, Z. F. Wu, P. F. Gao, S. L. Zhang and Y. H. Wen, *ACS Appl. Mater. Interfaces*, 2016, **8**, 22175–22181.
- J. C. Zheng and Y. Zhu, *Phys. Rev. B: Condens. Matter Mater. Phys.*, 2006, **73**, 24509.
- P. K. Sharma, A. Ruotolo, R. Khan, Y. K. Mishra, N. K. Kaushik, N. Y. Kim and A. K. Kaushik, *Mater. Lett.*, 2022, **308**, 131089.
- S. Yadav, M. A. Sadique, A. Kaushik, P. Ranjan, R. Khan and A. K. Srivastava, *J. Mater. Chem. B*, 2022, **10**, 1146.
- V. Chaudhary, A. Kaushik, H. Furukawa and A. Khosla, *ECS Sens. Plus*, 2022, **1**, 013601.
- P. K. Sharma, A. Ruotolo, R. Khan, Y. K. Mishra, N. K. Kaushik, N. Y. Kim and A. K. Kaushik, *Mater. Lett.*, 2022, **308**, 131089.
- A. J. Mannix, X. F. Zhou, B. Kiraly, J. D. Wood, D. Alducin, B. D. Myers, X. Liu, B. L. Fisher, U. Santiago and J. R. Guest, *Science*, 2015, **350**, 1513–1516.
- B. Feng, J. Zhang, Q. Zhong, W. Li, S. Li, H. Li, P. Cheng, S. Meng, L. Chen and K. Wu, *Nat. Chem.*, 2016, **8**, 563–568.
- R. Wu, A. Gozar and I. Božović, *npj Quantum Mater.*, 2019, **4**, 1–6.
- H. Li, L. Jing, W. Liu, J. Lin, R. Y. Tay, S. H. Tsang and E. H.-T. Teo, *ACS Nano*, 2018, **12**, 1262–1272.
- L. Ponomarenko, A. Geim, A. Zhukov, R. Jalil, S. Morozov, K. Novoselov, I. Grigorieva, E. Hill, V. Cheianov and V. Fal'Ko, *Nat. Phys.*, 2011, **7**, 958–961.
- R. Decker, Y. Wang, V. W. Brar, W. Regan, H. Z. Tsai, Q. Wu, W. Gannett, A. Zettl and M. F. Crommie, *Nano Lett.*, 2011, **11**, 2291–2295.
- L. Britnell, R. Gorbachev, R. Jalil, B. Belle, F. Schedin, A. Mishchenko, T. Georgiou, M. Katsnelson, L. Eaves and S. Morozov, *Science*, 2012, **335**, 947–950.
- W. Yang, G. Chen, Z. Shi, C. C. Liu, L. Zhang, G. Xie, M. Cheng, D. Wang, R. Yang and D. Shi, *Nat. Mater.*, 2013, **12**, 792–797.

- 25 C. C. Chen, Z. Li, L. Shi and S. B. Cronin, *Nano Res.*, 2015, **8**, 666–672.
- 26 X. Li, S. Lin, X. Lin, Z. Xu, P. Wang, S. Zhang, H. Zhong, W. Xu, Z. Wu and W. Fang, *Opt. Express*, 2016, **24**, 134–145.
- 27 X. Yang, F. Zhai, H. Hu, D. Hu, R. Liu, S. Zhang, M. Sun, Z. Sun, J. Chen and Q. Dai, *Adv. Mater.*, 2016, **28**, 2931–2938.
- 28 P. Kumar, J. Liu, M. Motlag, L. Tong, Y. Hu, X. Huang, A. Bandopadhyay, S. K. Pati, L. Ye and J. Irudayaraj, *Nano Lett.*, 2018, **19**, 283–291.
- 29 Z. Zhang, E. S. Penev and B. I. Yakobson, *Chem. Soc. Rev.*, 2017, **46**, 6746–6763.
- 30 Z. Zhang, Y. Yang, G. Gao and B. I. Yakobson., *Angew. Chem.*, 2015, **127**, 13214–13218.
- 31 J. Li, Q. Shi, Y. Zeng, K. Watanabe, T. Taniguchi, J. Hone and C. Dean, *Nat. Phys.*, 2019, **15**, 898–903.
- 32 R. Drost, A. Uppstu, F. Schulz, S. K. Hämäläinen, M. Ervasti, A. Harju and P. Liljeroth, *Nano Lett.*, 2014, **14**, 5128–5132.
- 33 B. Sachs, T. Wehling, M. Katsnelson and A. Lichtenstein, *Phys. Rev. B*, 2016, **94**, 224105.
- 34 S. K. Behera and P. Deb, *RSC Adv.*, 2017, **7**, 31393–31400.
- 35 J. P. Perdew, K. Burke and M. Ernzerhof, *Phys. Rev. Lett.*, 1996, **77**, 3865.
- 36 X. Liu and M. C. Hersam, *Sci. Adv.*, 2019, **5**, 6444.
- 37 J. Xue, J. S. Yamagishi, D. Bulmash, P. Jacquod, A. Deshpande, K. Watanabe, T. Taniguchi, P. J. Herrero and B. J. LeRoy, *Nat. Mater.*, 2011, **10**, 282–285.
- 38 K. Yonaga and N. Shibata, *J. Phys. Soc. Jpn.*, 2018, **87**, 034708.
- 39 Y. Cao, V. Fatemi, S. Fang, K. Watanabe, T. Taniguchi, E. Kaxiras and P. J. Herrero, *Nature*, 2018, **556**, 43–50.
- 40 N. R. Finney, M. Yankowitz, L. Muraleetharan, K. Watanabe, T. Taniguchi, C. R. Dean and J. Hone, *Nat. Nanotechnol.*, 2019, **14**, 1029–1034.
- 41 C. R. Dean, A. F. Young, I. Meric, C. Lee, L. Wang, S. Sorgenfrei, K. Watanabe, T. Taniguchi, P. Kim and K. L. Shepard, *Nat. Nanotechnol.*, 2010, **5**, 722–726.
- 42 Y. Wang, E. Liu, A. Gao, T. Cao, M. Long, C. Pan, L. Zhang, J. Zeng, C. Wang and W. Hu, *ACS Nano*, 2018, **12**, 9513–9520.
- 43 M. Koshino, *New J. Phys.*, 2015, **17**, 015014.
- 44 N. Levy, S. Burke, K. Meaker, M. Panlasigui, A. Zettl, F. Guinea, A. C. Neto and M. F. Crommie, *Science*, 2010, **329**, 544–547.
- 45 M. Motlag, P. Kumar, K. Y. Hu, S. Jin, J. Li, J. Shao, X. Yi, Y. H. Lin, J. C. Walrath and L. Tong, *Adv. Mater.*, 2019, **31**, 1900597.
- 46 L. Xu, W. Q. Huang, W. Hu, K. Yang, B. X. Zhou, A. Pan and G. F. Huang, *Chem. Mater.*, 2017, **29**, 5504–5512.
- 47 B. Cui, Y. Xing, J. Han, W. Lv, T. Lei, Y. Zhang, H. Ma, Z. Zeng and B. Zhang, *Chin. Phys. B*, 2021, **30**, 028507.
- 48 C. Jin, E. C. Regan, D. Wang, M. I.-B. Utama, C. S. Yang, J. Cain, Y. Qin, Y. Shen, Z. Zheng and K. Watanabe, *Nat. Phys.*, 2019, **15**, 1140–1144.
- 49 M. Y. Hassan and D. S. Ang, *ACS Appl. Mater. Interfaces*, 2019, **11**, 42339.
- 50 A. S. Chaves and H. Chacham, *Appl. Phys. Lett.*, 1995, **66**, 727.